RSC Advances

PAPER

View Article Online
View Journal | View Issue

Cite this: *RSC Adv.*, 2019, **9**, 8131

Enhanced photoluminescence of LEuH nanosheets: 2D photonic crystals self-assembled by core–shell SiO_2@LEuH spheres†

Xinying Wang,[a] Pingping Feng,‡[a] Baiyi Shao,[a] Fangming Cui*[b] and Xiaojing Yang *[a]

Received 22nd January 2019
Accepted 27th February 2019

DOI: 10.1039/c9ra00543a

rsc.li/rsc-advances

The enhancement in photoluminescence (PL) is a challenge for layered rare-earth hydroxides, which usually have weak PL due to the quenching effect of hydroxyls. In this work, we provide a strategy to enhance the PL behavior by constructing two-dimensional (2D) photonic crystals. The core–shell structured SiO_2@LEuH spheres were prepared by attaching the positively charged layered europium hydroxide (LEuH) nanosheets onto the negatively charged surfaces of the SiO_2 spheres; the core–shell spheres further formed a monolayered 2D colloidal crystal with the hexagonal lattice on a quartz substrate through an evaporation-induced assembly process. The 2D colloidal crystals exhibited a significantly enhanced photoluminescence at 611 nm related to the $^5D_0 \rightarrow {}^7F_2$ transition of Eu^{3+} compared with the SiO_2@LEuH spheres and the LEuH nanosheets dispersed in deionized water. The emission band of Eu^{3+} hardly changed in the three samples; therefore, the PL enhancement can be attributed to the emission band located at the short edge of the photonic band-gap of the 2D crystals.

Introduction

The synthesis,[1] structure[2] and exfoliation[3] of layered rare-earth hydroxide (LRH) nanosheets have been widely studied in the past decades due to their potential applications in absorption,[4] magnetism,[5] photoluminescence[6] (PL), *etc.* However, the PL intensity of LRHs is relatively weak compared with that of the rare-earth-doped ceramic materials due to the hydroxyl groups of LRHs. For the layered europium hydroxides (LEuHs), the $^5D_0 \rightarrow {}^7F_2$ transition at 615 nm of Eu^{3+} is largely derived from the C_1-site, while the $^5D_0 \rightarrow {}^7F_4$ transition at 698 nm is associated with the C_{4v}-site. In general, the luminescence enhancement of Eu^{3+} is mainly concentrated on the regulation of $^5D_0 \rightarrow {}^7F_2$.[7] In order to improve the PL performance of LRHs, various organic anions have been intercalated into the interlayers of LRHs based on the sensitization enhancement effect.[8–10] Other studies achieved the PL enhancement by converting LRHs into rare-earth oxides[11] *via* calcination or a topological reaction.[12] Byeon *et al.* prepared multi-colored LRH films *via* alternately stacking the LEuHs and LTbH nanosheets.[13] Hu *et al.* fabricated LRH films at the hexane/water interface.[14] All these works achieved enhanced PL performance through annealing at high temperatures to remove the hydroxyl groups. These works have focused more on adjusting the structure of LRHs instead of modifying their surrounding environment.

It is noticed that the two-dimensional (2D) monolayers of a polystyrene sphere on the phosphor film surface can improve the PL efficiency of the phosphor films.[15] Colloidal crystals have attracted intensive research attention owing to their high reproducibility, low cost and wide applications in electronics and optics.[16] The relationship between the photonic band-gap of the colloidal crystals and the PL of the rare-earth materials has been researched due to the narrow PL emission lines of rare earth elements compared with that of the photonic band-gap of the colloidal crystals.[17] Inverse opal structural materials of Eu^{3+}-doped Gd_2O_3,[17] Lu_2O_3,[18] YVO_4 (ref. 19) and $NaY(MoO_4)_2$ (ref. 20) have been prepared and their PL performance results show that the PL emission can be significantly suppressed when the emission bands overlap with the photonic band gap, whereas the enhancement in the emission occurs when the emission bands appear at the long edge of the photonic band gap. Furthermore, these results also showed that the $^5D_0 \rightarrow {}^7F_J$ radiative lifetimes of Eu^{3+} in the inverse opal structure prolonged and the concentration quenching of Eu^{3+} was suppressed. However, the influence of the photonic band-gap on opal structural materials is rarely reported; furthermore, the influence on the PL performance of LRHs has not been reported.

Herein, we attached LEuH nanosheets onto the surface of silica micro-spheres by phosphate modification, forming core–

[a]*Beijing Key Laboratory of Energy Conversion and Storage Materials, College of Chemistry, Beijing Normal University, 19-Xinjiekouwai Street, Haidian District, Beijing 100875, China. E-mail: yang.xiaojing@bnu.edu.cn*

[b]*Qian Xuesen Laboratory of Space Technology, China Academy of Space Technology, 104-Youyi Road, Haidian District, Beijing 100094, China*

† Electronic supplementary information (ESI) available. See DOI: 10.1039/c9ra00543a

‡ Present Address: Institute of Molecular Medicine, State Key Laboratory of Oncogenes and Related Genes, Shanghai Institute of Cancer, Renji Hospital, Shanghai Jiao Tong University School of Medicine, School of Chemistry and Chemical Engineering, Shanghai Jiao Tong University, Shanghai 200240, China.

shell-structured SiO_2@LEuH micro-spheres, which were further self-assembled into a mono-layered 2D colloidal crystal with a hexagonal lattice on a quartz substrate through an evaporation-induced assembly process. The mono-layered 2D colloidal crystal showed improved PL performance due to the effects of the photonic band gap on the PL emission of LEuHs.

The motive to study such a material is that we consider that it may have three merits: first, it would provide a new method to "solidify" the nanosheets of LRHs; second, we can provide a strategy to enhance the PL intensity of LRHs without any further chemical treatments, such as annealing at high temperatures or topological reactions; third, this study would enrich the work on the influence of the photonic band gap on the opal structural materials.

Experimental

Materials

Eu_2O_3 (99.9%), KOH and SiO_2 spheres (1 μm) were purchased from Shanghai Aladdin Biochem Technology Co., Ltd; TSPMP was purchased from HEOWNS Biochem Technologies, LLC.

Preparation of LEuH nanosheets

The $Eu(NO_3)_3 \cdot 6H_2O$ powder was first prepared as follows: 3 g Eu_2O_3 (99.9%) was added into aqueous HNO_3 solution and then, the solution was heated in an oil bath at 80 °C for 3 h under stirring. After that, the $Eu(NO_3)_3 \cdot 6H_2O$ powder was obtained by filtration and drying.

The LEuH nanosheets were prepared according to a reported method.[21] Typically, 50 mL 0.10 M aqueous KOH solution was added dropwise to 50 mL 0.05 M aqueous $Eu(NO_3)_3 \cdot 6H_2O$ solution under vigorous stirring at room temperature and kept for 12 h. The precipitate was collected by centrifugation and washed with deionized water several times. A slurry of the LEuH nanosheets was redispersed into deionized water by sonication to prepare a 0.2 g L^{-1} aqueous LEuH suspension.

Preparation of core–shell structured SiO_2@LEuH spheres

First, the SiO_2 spheres were modified with phosphate through mixing and reaction of 0.025 g SiO_2 spheres and 0.5 mL sodium(3-(trihydroxysilyl)propyl)methylphosphonate (TPMP) in 40 mL water and 10 mL ethanol mixture for 5 hours. Second, the phosphate-modified SiO_2 spheres were collected by centrifugation and washing. Third, the LEuH nanosheets were attached to the surface of SiO_2 spheres by re-dispersion of the modified SiO_2 spheres into 100 mL LEuH aqueous solution and stirring for 1 hour. Finally, the resulting core–shell-structured SiO_2@LEuH spheres were obtained by centrifugation at 6000 rpm for 3 min.

Preparation of 2D colloidal crystals of SiO_2@LEuHs

The 2D colloidal crystals of SiO_2@LEuHs were prepared by an evaporation-induced assembly process. First, 3 mL aqueous SiO_2@LEuH solutions with different SiO_2@LEuH contents, *i.e.*, 0.0002, 0.002, 0.004, 0.006, 0.008, 0.01 and 0.012 wt% and 3 mL water–ethanol mixtures with different ethanol volume fractions for tuning the surface tension were prepared, as seen from the data in Table 1. Second, the clean quartz substrates were immersed vertically into the prepared solutions and the mixtures were kept at 40 °C for solvent evaporation. Finally, the substrates were taken out after the solvent evaporated and dried at an ambient temperature. The 3D arrays and 2D colloidal crystals of SiO_2@LEuHs were then deposited on the substrates.

Table 1 Features of different solutions for the preparation of the 2D colloidal crystals of SiO_2@LEuHs[a]

Solutions	V (%)	σ (N m^{-1})
Sol. 1	0	71.5
Sol. 2	20	41.8
Sol. 3	33	36.0
Sol. 4	50	30.7
Sol. 5	67	27.3
Sol. 6	80	25.5

[a] V: ethanol volume fraction of the aqueous solutions, σ: surface tension of the solutions.

Characterization

X-ray diffraction (XRD) measurements were carried out using a Phillips X'Pert Pro MPD diffractometer with Cu-Kα radiation ($\lambda = 0.1541$ nm) at room temperature (40 kV, 40 mA, 10 s per step) and a step size of 0.017°. Scanning electron microscopy (SEM) images were obtained using a model S-4800 microscope (Hitachi, Ltd.) with an accelerating voltage of 5.0 kV. The surface tension of the solutions was measured by BCZ-600 with the resolution of 0.1 mN m^{-1} at room temperature. A transmission spectrum was measured under the 'Transmittance' mode by a SHIMADZU UV-2600 spectrophotometer. The slit width was set as 2 nm; the sweeping was set under a low speed and the sampling interval was set as 1 nm s^{-1}. Excitation and emission spectra of the photoluminescence were measured by an FS5 fluorescence spectrophotometer with slit width of 5 nm and the incident light vertical to the substrates. The elemental mapping was carried out by energy dispersive X-ray spectroscopy under a TEM scanning model.

Results and discussion

Scheme 1 shows a schematic for the formation process of the 2D colloidal crystals of the core–shell-structured SiO_2@LEuHs. First, the surfaces of SiO_2 spheres were modified with negatively charged phosphate ions by TSPMP. Then, the LEuH nanosheets were absorbed and adhered on the surface of the modified SiO_2 spheres through the electrostatic interaction between the positive LEuH nanosheets and the negative phosphate ions on the SiO_2 sphere surfaces; this is certified by the results of the zeta-potentials of the samples in Fig. S1.† Finally, the 2D colloidal crystals of the core–shell-structured SiO_2@LEuHs were prepared and deposited on the quartz substrates *via* an evaporation-induced assembly process under the action of capillary forces.

The XRD patterns of the samples are shown in Fig. 1. The original LEuH nanosheets present two sharp diffraction peaks at $2\theta = 9.65$ and 19.46°, corresponding to the (002) and (004)

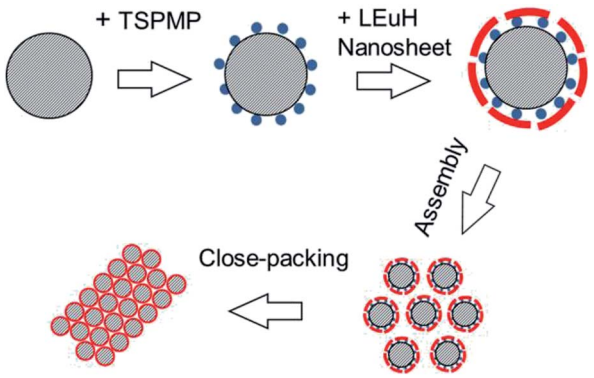

Scheme 1 A schematic for the formation of the 2D colloidal crystals of the core–shell-structured SiO_2@LEuHs.

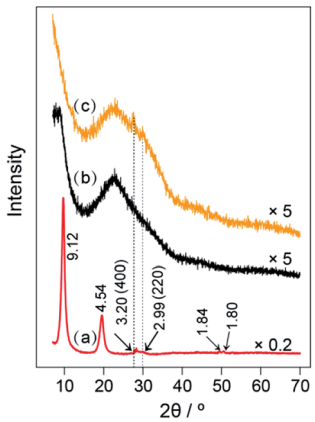

Fig. 1 XRD patterns of (a) LEuH nanosheets, (b) SiO_2 spheres and (c) the core–shell-structured SiO_2@LEuHs.

planes of the LEuH nanosheets and indicating the well-ordered hydroxide layers, as seen in curve (a) of Fig. 1.[22,23] The plane distances are 9.1 and 4.54 Å, which are consistent with our previous results.[24] The wide diffraction peak around 23° in curve (b) of Fig. 1 can be attributed to the diffraction of amorphous silica of SiO_2 spheres. The core–shell-structured SiO_2@LEuHs show two weak diffraction peaks at $2\theta = 28$ and 30°, as seen in curve (c) of Fig. 1, which can be indexed as the (400) and (220) intra-layer planes of the LEuH nanosheets, respectively, and are consistent with the diffractions of the original LEuH nanosheets, as indicated by two vertical dot lines. Meanwhile, the core–shell-structured SiO_2@LEuHs do not show the diffraction peaks of the (002) and (004) planes of the LEuH nanosheets again, which is due to the dramatic reduction in the number of layers of the LEuH nanosheets along the *c*-axis, indicating the monolayer or few-layer attachment of LEuH nanosheets onto the surface of SiO_2 spheres. The thickness of the nanosheets after ultra-sonication was measured as 5.45 nm (Fig. S2†), indicating that the nanosheets comprise few layers.

The TEM images of the prepared LEuH nanosheets are shown in Fig. 2, and they present the layer structured nanosheets with 2D size at ~200 nm; europium homogeneously disperses in the nanosheet area, which indicates the good integrity of the LEuH

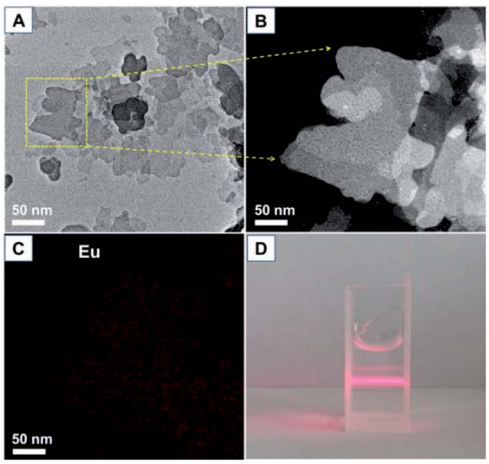

Fig. 2 (A) TEM image of the prepared LEuH nanosheets, (B) enlarged dark-field TEM image of the selected area, (C) europium mapping and (D) optical picture of the aqueous LEuH solution.

nanosheets and homogeneous composition, as seen in Fig. 2(C). The aqueous LEuH solution presents an obvious Tyndall effect under red laser irradiation, indicating the good dispersion of the LEuH nanosheets in water, as seen in Fig. 2(D).

The microstructure and elemental mapping of the core–shell-structured SiO_2@LEuH spheres were characterized by SEM and TEM, as shown in Fig. 3. The SiO_2 spheres present a smooth surface and uniform diameter of ~1 μm, as seen in Fig. 3(A). The phosphate-modified SiO_2 spheres pack more closely on the SEM sample support maybe due to the surface functional molecules and show the same diameter of ~1 μm as the unmodified SiO_2 spheres, as seen in Fig. 3(B). The core–shell-structured SiO_2@LEuH spheres present rough surfaces compared with the two formers, as seen in Fig. 3(C), which are due to the attached LEuH nanosheets on the surface of the SiO_2 spheres. Furthermore, the surface-attached LEuH nanosheets can be clearly seen from the TEM image of a single core–shell-

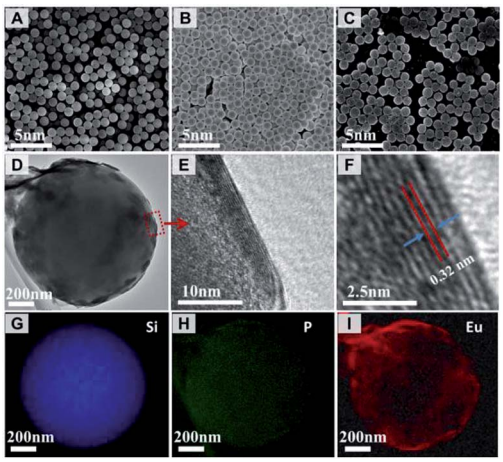

Fig. 3 SEM images of (A) SiO_2, (B) modified SiO_2 and (C) core–shell-structured SiO_2@LEuH spheres; TEM images of (D) single, (E and F) enlarged edge of SiO_2@LEuH sphere; TEM elemental mapping of (G) silicon, (H) phosphorous and (I) europium for a single SiO_2@LEuH sphere.

structured SiO_2@LEuH sphere in Fig. 3(D). The enlarged TEM image at an arbitrary edge and the surface of a single SiO_2@LEuH sphere, indicated by the red rectangle in Fig. 3(D), clearly show the laminar lattice fringes of the LEuH nanosheets with a spacing of 0.32 nm, which is consistent with the distance of the (400) intra-layer planes of the LEuH nanosheets characterized by above XRD, as seen in Fig. 3(E) and (F). The TEM elemental mapping results of a single SiO_2@LEuH sphere, shown in Fig. 3(G)–(I), give more evidence of the core–shell structure of the SiO_2@LEuH sphere. The homogeneous distribution of phosphorous and europium on/around the surface of the SiO_2 sphere indicates the complete modification of phosphate and the coating of the LEuH nanosheets on the surface of the SiO_2 sphere.

The 2D colloidal crystals of SiO_2@LEuHs were prepared by an evaporation-induced assembly process, and the preparation process was not as easy as that of smooth SiO_2 spheres because of the rough surface of the core–shell-structured SiO_2@LEuH spheres. Here, both the SiO_2@LEuH content in the water–ethanol solutions and the surface tension of the solutions were important. We first prepared the arrays of SiO_2@LEuHs on quartz substrates from a series of solutions with different SiO_2@LEuH contents and found out an optimal and appropriate SiO_2@LEuH content of 0.008 wt% for the periodic 2D colloidal crystal preparation, as seen in the SEM images in Fig. S3.† Second, the surface tension of the SiO_2@LEuH solution was tuned by changing the ethanol volume fraction of the solution, as shown in Table 1. The surface tension (σ) decreases as V increases due to the smaller surface tension of ethanol than that of deionized water, and σ falls sharply before 20%, which is consistent with previous results.[25]

Fig. 4 shows the SEM images of the 2D colloidal crystals of the core–shell-structured SiO_2@LEuHs prepared from aqueous solutions with different ethanol volume fractions at 0.008 wt% SiO_2@LEuH content. The 2D colloidal crystals of SiO_2@LEuHs prepared from Sol. 3 presented the best 2D periodic morphology with uniform monolayers and few vacancies compared with others, as seen in Fig. 4(C).

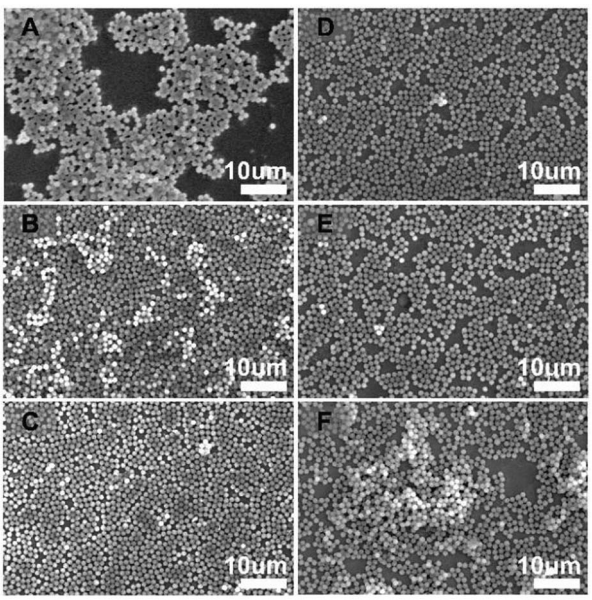

Fig. 4 SEM images of the 2D colloidal crystals of SiO_2@LEuHs prepared from different solutions: (A) Sol. 1, (B) Sol. 2, (C) Sol. 3, (D) Sol. 4, (E) Sol. 5 and (F) Sol. 6.

Whether the spheres arrange closely and uniformly depends on the infiltration degree of the liquid to the quartz surface and the matching degree of the surface energies between the liquid and the spheres. When the volume fraction of ethanol is 20%, σ of the liquid drops rapidly and then slowly with continuous increments in the volume fraction. This could be because the liquid can completely infiltrate the quartz surface when the volume fraction is 20%. As the liquid is water, σ of the liquid is equal to that of water, and the liquid cannot completely infiltrate the surface of quartz. At the same time, the surface energy of the liquid is higher than that of the spheres, and the above two factors both result in the presence of obvious local 3D packing of the spheres, as seen in Fig. 4(A). As the volume fraction of ethanol increases, the surface energy of the liquid gradually approaches that of the spheres, and the agglomeration phenomenon is weakened. When the volume fraction reaches 33%, the surface energy of the liquid is closest to that of the spheres, leading to monolayer close packing (Fig. 4(C)). On further increasing the volume fraction of ethanol, the surface energy of the liquid becomes lower than that of the spheres, leading to the presence of vacancies and agglomeration, as seen in Fig. 4(D)–(F). Meanwhile, the faster evaporation rate of the liquid leads to significant agglomeration (Fig. 4(F)) compared with the observations obtained from Fig. 4(D) and (E).

Generally, in photonic crystals, the change in the PL behavior of Eu^{3+} could be explained by a variety of reasons. First, as the emission band lies in the range of the band gap, the change in the PL behavior is mainly ascribed to the photonic band-gap effects: (1) significant suppression of the emission will be detected if the photonic band-gap overlaps with the rare-earth emission bands;[26] (2) enhancement in the emission is attributed to the standing wave effects. Galstyan *et al.* proposed a model where the standing wave effects determine the enhancements at the edges of the photonic band-gap,[27] as seen in Table 2. In the opal system, as the emission band lies at the short wavelength edge of the photonic band-gap, where the standing wave corresponds to a position at the pole, the photoluminescence is enhanced. For the inverse opal system, as the emission band lies at the long wavelength edge of the photonic band-gap, where the standing wave corresponds to a position at the pole, the photoluminescence is also enhanced. Second, as the emission band lies out of the range of the photonic band-

Table 2 Summary about the effects of photonic band-gap on spontaneous emissions

Position of emission bands	Inverse opal	Opal
Center	Suppression	Suppression
Long-wavelength edge	Enhancement[a]	Suppression[b]
Short-wavelength edge	Suppression[b]	Enhancement[a]

[a] The standing wave lies at the pole. [b] The standing wave lies at the equator.

gap, (1) the suppression of the emission is ascribed to the higher site symmetry of Eu^{3+} ions compared with that of the precursor[17] and (2) the enhancement of the PL properties is ascribed to the higher effective refractive indices that minimize the surface scattering of both the excitation and emission lights after close packing of the core–shell structures.[8]

In this experiment, we synthesized a periodic hexagonal close-packed single layer parallel to the laminate, and it was considered that a photonic band gap would be present in the direction parallel to the laminate rather than in the direction perpendicular to the laminate. Fig. 5(A) shows the transmission spectrum with light parallel to the direction of the laminate. This stop-band is centred at 660 nm.

Theoretically, the position of the photonic band-gap in photonic crystals can be estimated by the Bragg's law of diffraction combined with the Snell's law.[7]

$$\lambda_{PBG} = 2d_{hkl}\sqrt{{n_{eff}}^2 - \sin\theta^2} \quad (1)$$

$$n_{eff} = n_{spheres}\phi + n_{air}(1 - \phi) \quad (2)$$

Here, λ_{PBG} is the centre of the band-gap, d_{hkl} is the *hkl* plane distance, n_{eff} is the average refractive index ($n_{sphere} = 1.364$), θ is the angle from the incident light to the normal of the substrate surface, and ϕ is the volume fraction of the spheres ($\phi = 0.74$). In this discussion, the monolayer is considered as the (111) plane of the face-centred cubic (fcc) phase due to the higher stability of the fcc phase compared with that of the hexagonal closed-packed (hcp) phase,[28] and any plane perpendicular to the (111) plane will produce a stop-band gap. A series of planes with $d_{hkl} = 0.26D$ (D is the diameter of the spheres) were found within the monolayer, as seen in Fig. 6, and λ_{PBG} was calculated to be 660 nm, which was consistent with the experimental results. It is worth noting that in this work, the calculation result is a case under certain conditions and is just used to verify our experimental results.

The PLE curve (a) in Fig. 5 shows an excitation peak at 394 nm, and curves (b) and (c) show an excitation peak at 248 nm. The PL curve (a) and curves (b) and (c) present the characteristic $^5D_0 \rightarrow {}^7F_J$ ($J = 2, 3, 4$) transitions of Eu^{3+} under excitations of 394 nm and 248 nm, respectively. The PL behavior

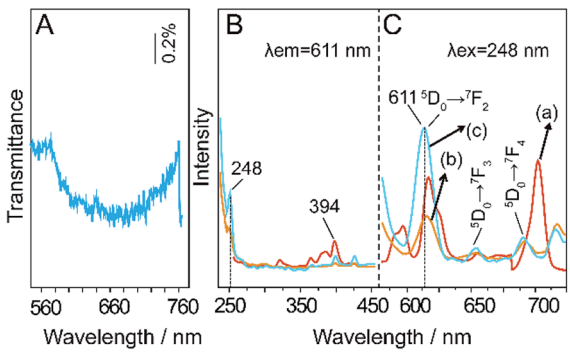

Fig. 5 (A) Transmission spectra of 2D colloidal crystals of SiO_2@LEuHs; (B) and (C) PLE and PL spectra of (a) LEuHs, (b) SiO_2@LEuHs and (c) 2D colloidal crystals of SiO_2@LEuHs.

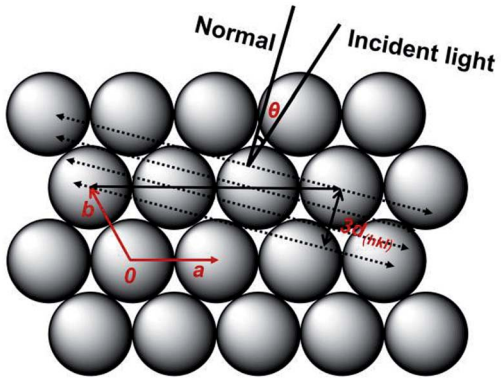

Fig. 6 Schematic diagram of the formation of the stop-band gap as the incident light parallels to the (111) plane of the fcc phase.

of $^5D_0 \rightarrow {}^7F_{2,4}$ will be discussed due to the obvious changes. According to a previous report, the theoretical calculation result of the relative photonic band-gap width, $\Delta\lambda/\lambda_0$, for an fcc phase, where $\Delta\lambda$ is the width at half-maximum of the peak and λ_0 is the centre wavelength of the peak, is 7%;[29] we can establish that the transition $^5D_0 \rightarrow {}^7F_2$ (611 nm) of Eu^{3+} lies in the short range of the stop-band gap and the transition $^5D_0 \rightarrow {}^7F_2$ (690 nm) of Eu^{3+} overlaps with the stop-band gap. As seen from the figures, first, the PL intensity of $^5D_0 \rightarrow {}^7F_2$ of the mono-layered 2D photonic crystals with the hexagonal lattice is significantly enhanced compared with those of the LEuH nanosheets and the core–shell-structured SiO_2@LEuH spheres. For this opal system, the $^5D_0 \rightarrow {}^7F_2$ transition at 611 nm lies in the short range of the stop-band gap, where the standing wave corresponds to a position at the pole, which results in the photoluminescence enhancement. Second, the PL intensity of the $^5D_0 \rightarrow {}^7F_4$ transition at ~690 nm of the periodic monolayer decreases compared with that of the LEuH nanosheets due to the overlap of $^5D_0 \rightarrow {}^7F_4$ with the stop-band gap. Meanwhile, the $^5D_0 \rightarrow {}^7F_{2,4}$ transitions of Eu^{3+} are electric-dipole allowed and their intensities are sensitive to the local structure surrounding the Eu^{3+} ions. The higher site symmetry of the Eu^{3+} ions leads to the suppression of $^5D_0 \rightarrow {}^7F_{2,4}$ of the core–shell-structured SiO_2@LEuHs compared with that observed for the LEuH nanosheets. Overall, as seen from the enhanced PL of the typical $^5D_0 \rightarrow {}^7F_2$ transition and the higher PL intensity of the periodic monolayer compared with those of the other samples, it can be considered that the enhancement in the photoluminescence of LEuHs is achieved *via* the modification of the photonic crystal structures.

It is worth noting that to the best of our knowledge, this would be the first report on the photoluminescence enhancement of LRHs due to the modification of the photonic crystal structures; this would also be the first report of a method of enhancing the photoluminescence of the LRHs without any chemical treatments such as calcination or topology reactions.

Conclusions

In this paper, we synthesized the core–shell structures of rare-earth hydroxide nanosheets and further formed a mono-

layered 2D colloidal crystal with a hexagonal lattice on a quartz substrate through an evaporation-induced assembly process. First, the most important aspect is that for the first time, we introduced LRHs into the photonic crystals and achieved enhancement in the photoluminescence of LRHs without any further chemical treatments. This provides a strategy to enhance the photoluminescence of LRHs. Second, obtaining a mono-layered 2D photonic crystal provides a novel method to solidify the rare-earth hydroxide nanosheets. Third, the modification of the photonic crystals for the spontaneous emission of Eu^{3+} would enrich the study of the effects of the photonic crystal structures on opal structures.

Conflicts of interest

There are no conflicts to declare.

Acknowledgements

This work was supported by the National Science Foundation of China (Grants. 51572031 and 51272030), and Program for Changjiang Scholars and Innovative Research Team in University.

References

1 F. Geng, Y. Matsushita, R. Ma, H. Xin, M. Tanaka, N. Iyi and T. Sasaki, *Inorg. Chem.*, 2009, **48**, 6724–6730.
2 F. Geng, Y. Matsushita, R. Ma, H. Xin, M. Tanaka, F. Izumi, N. Iyi and T. Sasaki, *J. Am. Chem. Soc.*, 2008, **130**, 16344–16350.
3 L. Hu, R. Ma, T. C. Ozawa and T. Sasaki, *Chem.–Asian J.*, 2010, **5**, 248–251.
4 C. C. L. Pereira, J. C. Lima, A. J. Moro and B. Monteiro, *Appl. Clay Sci.*, 2017, **146**, 216–222.
5 Y.-s. Yoon, B.-I. Lee, K. S. Lee, G. H. Im, S.-H. Byeon, J. H. Lee and I. S. Lee, *Adv. Funct. Mater.*, 2009, **19**, 3375–3380.
6 B.-I. Lee and S.-H. Byeon, *Chem. Commun.*, 2011, **47**, 4093–4095.
7 Q. Zhu, J.-G. Li, C. Zhi, X. Li, X. Sun, Y. Sakka, D. Golberg and Y. Bando, *Chem. Mater.*, 2010, **22**, 4204–4213.
8 Q. Gu, N. Chu, G. Pan, G. Sun, S. Ma and X. Yang, *Eur. J. Inorg. Chem.*, 2014, 559–566.
9 W. Li, Q. Gu, F. Su, Y. Sun, G. Sun, S. Ma and X. Yang, *Inorg. Chem.*, 2013, **52**, 14010–14017.
10 Q. Gu, F. Su, L. Ma, S. Ma, G. Sun and X. Yang, *J. Mater. Chem. C*, 2015, **3**, 4742–4750.
11 Q. Zhu, J. G. Li, C. Zhi, R. Ma, T. Sasaki, J. X. Xu, C. H. Liu, X. D. Li, X. D. Sun and Y. Sakka, *J. Mater. Chem.*, 2011, **21**, 6903.
12 B. Shao, Q. Zhao, W. Lv, M. Jiao, W. Lü and H. You, *J. Mater. Chem. C*, 2015, **3**, 1091–1098.
13 B.-I. Lee, E.-s. Lee and S.-H. Byeon, *Adv. Funct. Mater.*, 2012, **22**, 3562–3569.
14 L. Hu, R. Ma, T. C. Ozawa and T. Sasaki, *Angew. Chem.*, 2009, **48**, 3846–3849.
15 K. Y. Ko, K. N. Lee, Y. K. Lee and Y. R. Do, *J. Phys. Chem. C*, 2008, **112**, 7594–7598.
16 C. Li, G. Hong and L. Qi, *Chem. Mater.*, 2010, **22**, 476–481.
17 X. Qu, H. K. Yang, B. K. Moon, B. C. Choi, J. H. Jeong and K. H. Kim, *J. Phys. Chem. C*, 2010, **114**, 19891–19894.
18 Y. Wang, Y. Zhu, W. Xu, H. Song, S. Xu, J. Wang and H. Cui, *Dalton Trans.*, 2013, **42**, 14014–14020.
19 Y. Zhu, W. Xu, H. Zhang, W. Wang, L. Tong, S. Xu, Z. Sun and H. Song, *Appl. Phys. Lett.*, 2012, **100**, 081104.
20 S. Cui, Y. Zhu, W. Xu, P. Zhou, L. Xia, X. Chen, H. Song and W. Han, *Dalton Trans.*, 2014, **43**, 13293–13298.
21 H. Jeong, B. I. Lee and S. H. Byeon, *Dalton Trans.*, 2012, **41**, 14055–14058.
22 K.-H. Lee and S.-H. Byeon, *Eur. J. Inorg. Chem.*, 2009, 929–936.
23 F. Geng, Y. Matsushita, R. Ma, H. Xin, M. Tanaka, N. Iyi and T. Sasaki, *Inorg. Chem.*, 2009, **48**, 6724–6730.
24 P. Feng, X. Wang, Y. Zhao, D. Fang and X. Yang, *RSC Adv.*, 2018, **8**, 3592–3598.
25 L. Zhu, Z. Zheng, Y. Zhang and Y. Jin, *Res. Explor. Lab.*, 2012, **31**, 58–61.
26 S. G. Romanov, A. V. Fokin and R. M. De La Rue, *Appl. Phys. Lett.*, 2000, **76**, 1656–1658.
27 A. G. Galstyan, M. E. Raikh and Z. V. Vardeny, *Phys. Rev. B: Condens. Matter Mater. Phys.*, 2000, **62**, 1780–1786.
28 L. V. Woodcock, *Nature*, 1997, **385**, 141–143.
29 Z.-Z. Gu, A. Fujishima and O. Sato, *Chem. Mater.*, 2002, **14**, 760–765.

